Earthquakes and Structures, *Vol. 7, No. 4 (2014) 463-484*
DOI: http://dx.doi.org/10.12989/eas.2014.7.4.463

Experimental investigations of the seismic performance of bridge piers with rounded rectangular cross-sections

Guangqiang Shao*[1], Lizhong Jiang[1,2a] and Nawawi Chouw[3b]

[1]*School of Civil Engineering*, *Central South University*, *22 Shaoshan South Road*, *Changsha*, *China*,
[2]*National Engineering Laboratory for Construction Technology of High Speed Rail*,
22 Shaoshan South Road, *Changsha*, *China*,
[3]*Department of Civil and Environmental Engineering*, *the University of Auckland*,
20 Symonds Street, *Auckland*, *New Zealand*

(Received February 25, 2014, Revised August 1, 2014, Accepted October 8, 2014)

Abstract. Solid piers with a rounded rectangular cross-section are widely used in railway bridges for high-speed trains in China. Compared to highway bridge piers, these railway bridge piers have a larger cross-section and less steel reinforcement. Existing material models cannot accurately predict the seismic behavior of this kind of railway bridge piers. This is because only a few parameters, such as axial load, longitudinal and transverse reinforcement, are taken into account. To enable a better understanding of the seismic behavior of this type of bridge pier, a simultaneous influence of the various parameters, i.e. ratio of height to thickness, axial load to concrete compressive strength ratio and longitudinal to transverse reinforcements, on the failure characteristics, hysteresis, skeleton curves, and displacement ductility were investigated. In total, nine model piers were tested under cyclic loading. The hysteretic response obtained from the experiments is compared with that obtained from numerical studies using existing material models. The experimental data shows that the hysteresis curves have significantly pinched characteristics that are associated with small longitudinal reinforcement ratios. The displacement ductility reduces with an increase in ratio of axial load to concrete compressive strength and longitudinal reinforcement ratio. The experimental results are largely in agreement with the numerical results obtained using Chang-Mander concrete model.

Keywords: RC railway bridge pier; cyclic loading; seismic performance; numerical analysis; displacement ductility

1. Introduction

The use of high-speed rail is increasing year by year in China. The proportion of bridge length to total track length is relative high in newly operated railway for high-speed trains. For example, the proportion is above 80% in the Beijing-Shanghai and Beijing-Tianjin high-speed rail lines (Zheng 2008). Many Chinese railway tracks for both high-speed and conventional rail are located in earthquake-prone regions. Research on the seismic performance of railway piers has not been

*Corresponding author, Ph.D. Candidate, E-mail: sgq608@gmail.com
[a]Professor, E-mail: lzhjiang@mail.csu.edu.cn
[b]Associate Professor, E-mail: n.chouw@auckland.ac.nz

http://www.techno-press.org/?journal=eas&subpage=7 ISSN: 2092-7614 (Print), 2092-7622 (Online)

conducted sufficiently. The limited number of seismic investigation reports indicated that the failure of bridges in earthquakes were mostly due to the failure of the substructure, through pier cracking, reinforcement buckling, and the tensile fracture of stirrups (e.g., Chen and Duan 2003). Consequently, more detailed investigation of the seismic behavior of railway bridge piers is necessary.

Experimental and theoretical studies on the seismic performance of solid bridge piers were performed by a number of researchers. For example, Mander *et al*. (1983) carried out an experimental investigation on ductile reinforced concrete bridge piers. After extensive experiments using low cyclic loading, Priestley and Park (1987) proposed a new design method for predicting the flexural strength and ductility of confined RC bridge columns. Belarbi *et al*. (2009) tested seven columns under cyclic flexural, shear and torsional loadings. The results showed that the combined loading reduced both the flexural and torsional capacities. Sigmund and Penava (2014) presented the experimental results of a study on RC frames infilled with masonry with openings. The research shows that factors influencing the seismic response are the ratio of axial load to concrete compressive strength, longitudinal reinforcement ratio, stirrup-to-concrete volume ratio and ratio of height to thickness of piers.

Uniaxial constitutive models were proposed for concrete core confined by steel reinforcement in circular or square RC piers under cyclic loading. Kent and Park (1971) described a simple uniaxial model of concrete, and then the model was improved by Scott *et al*. (1982) and widely used. Mander *et al*. (1988) proposed a stress-strain approach for a confined concrete based on an equation suggested by Popovics (1973). Chang and Mander (1994) extended the Mander model. Waugh (2009) has later improved the model. Braga *et al*. (2006) presented an analytical model to determine the confining pressures of transverse reinforcements on the concrete core. D'Amato *et al*. (2012) proposed a numerical model for a simulation of confinement effects. Osorio *et al*. (2012) performed experiments on cylindrical specimens under uniaxial cyclic compression and formulated an analytical model to obtain the lateral deformations of concrete. These uniaxial compression models have been continually improved to analyze concrete with different compressive strengths and reinforcement confinement. These models might be applied to the bridge piers for high-speed rails. However, a validation is required before they can be reliably used.

When it comes to the design of bridge piers, there are different considerations depending on the usage, i.e. in highway, conventional railway and railway for high-speed trains. Compared with highway bridge piers, the requirements of the railway bridge piers for high-speed trains are more complex. They demand higher longitudinal and lateral stiffness to ensure a comfortable and stable train ride. Consequently, a larger width and thickness due to the demand for high stiffness in both directions is required in railway bridge piers. The longitudinal reinforcement ratio of bridge piers is usually around 0.2% when the pier is to be constructed in a non-seismic region and is around 0.5-1% when the pier is to be constructed in a seismic region. This low percentage of reinforcement, i.e. 0.5-1%, presents a challenge to the designer in terms of satisfying the various seismic detailing requirements (Jia 2008). For an economical design, one option is to reduce the cross-section in order to have a high steel ratio to satisfy all these requirements. However, this may lead to a lower stiffness which may not be desirable. There is a need to find a balance between the required stiffness, aspect ratio, and longitudinal reinforcement ratio.

Currently, the bridge piers for Chinese high-speed rail follow the designs in Europe, Japan, or South Korea. The cross-sections of piers include rectangular hollow piers, oval hollow piers,

rounded rectangular solid piers, wall-type piers, single cylindrical piers and double-column piers. However, the same design regulations are applied for different kinds of piers, which is not reasonable.

Research on the seismic performance of railway bridge piers with low percentages of longitudinal reinforcements is very limited. Almost all tested piers so far were circular, octagonal, rectangular, or square in cross-sections. In the database of the Pacific Earthquake Engineering Research Center (PEER), the reinforcement of rectangular bridge piers was around 2.39%, with a tendency toward the lower reinforcement ratios. The distribution of transverse reinforcement ratio is weighted around 2%. Compared with the rectangular piers, nearly 50% of the spiral reinforced piers have a transverse reinforcement ratio between 0.5% and 1.0% (Berry *et al*. 2004). However, so far only a few test data of RC bridge piers with rounded rectangular (oval) cross-sections under cyclic loading have been reported. Fujikura *et al*. (2000) studied the strength and ductility of three piers with rounded rectangular cross-section by pseudo-static test to compare the effect of interlocking ties and cross ties. The longitudinal reinforcement ratios are around 0.8%. The results showed that the ductility of piers with the interlocking circle ties were better than the other two piers with the common spirals. Ju (2004) carried out pseudo-dynamic tests on conventional railway bridge piers with oval cross-sections taking into consideration height to shorter thickness and longitudinal reinforcement ratios. The results showed that the ductility of piers with lower reinforcement ratios is still satisfactory. However, the tests did not consider the imposed axial load which can affect the ductility considerably. Jia (2008) established finite element models for railway bridge piers for high-speed trains with oval cross-sections including the pile and subsoil and analyzed the influence on the displacements and internal forces of piers and girders. The author has also proposed some seismic design recommendations for pier construction to avoid pile group yielding prior to individual pier yielding. Jia and Dai (2012) analyzed the hysteretic curves of 4 rounded rectangular piers with HRBF 500 steel bars by finite element package ABAQUS under low cyclic loading.

To the authors' knowledge, the available studies did not describe the seismic behavior of railway piers for high-speed trains accurately. This is because only a few parameters (e.g. either axial-load ratio, longitudinal or transverse reinforcement) were taken into account. In this study, to understand the seismic behaviour of piers of railway bridges, the influence of the parameters on the failure characteristics, hysteresis curves, skeleton curves and displacement ductility is investigated. The considered parameters are the ratio of height to thickness, axial load to concrete compressive strength, longitudinal and transverse reinforcement ratio. In addition, the effectiveness of existing concrete models proposed by Kent-Scott-Park, Mander and Chang-Mander is evaluated.

2. Experimental procedures

2.1 Scaling of test specimens

For laboratory tests, the cross-sections of the bridge piers were scaled because of actuator limitations. When the actual pier height is less than 15 m, a geometry scale of 1:5 is used. A scale of 1:8 is used when the height ranges between 15 m and 25 m. The cross-sections of the prototype piers (indicated as P1 and P2) and model piers (named as S1 and S2) are shown in Fig.1. The

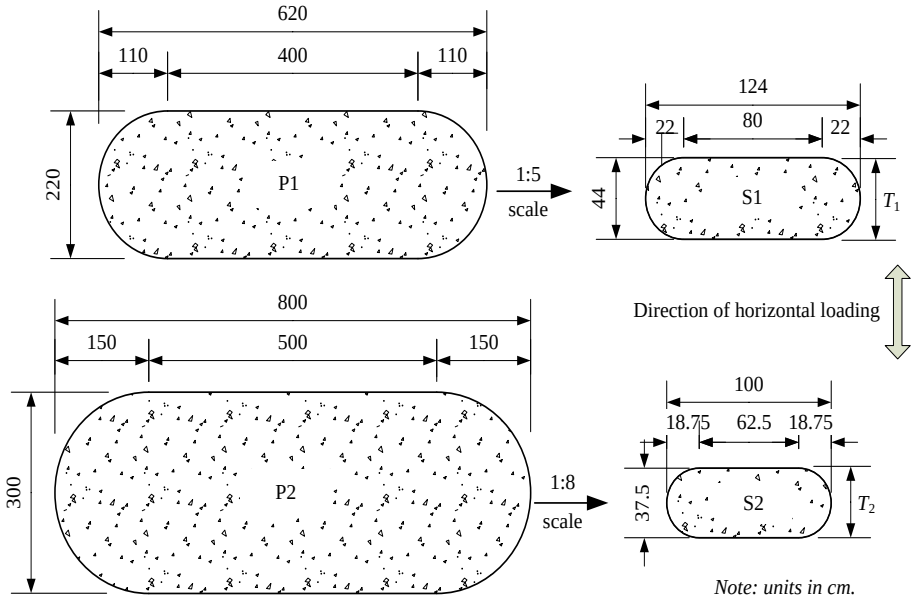

(a) Prototype piers (b) Model piers

Fig. 1 Dimension of the cross-sections

cross-sections of prototype are selected based on the pier height. In total nine specimens were tested under cyclic loading. They are grouped according to their heights of 1.6 m, 2 m and 3 m. The group with 1.6 m height is of S1 cross-section while other groups have S2 cross-sections. T_1 and T_2 represent the thickness of cross-sections along the horizontal loading direction.

2.2 Considered variables and selected combinations

The main variables affecting the pier failure modes include ratio of axial load to concrete compressive strength, longitudinal reinforcement ratio ρ_s, stirrup-to-concrete volume ratio ρ_v, aspect ratio λ, i. e. height H to thickness T. The concrete compressive strength of all specimens is 35 MPa, because it is widely used in railway bridge piers for high-speed trains. Based on previous studies of bridge piers under earthquake loading, usually the axial load ratio, the longitudinal reinforcement ratio and the stirrup-to-concrete volume- ratio are respectively less than 15%, 1% and 0.5% (e.g., Ju 2004). The variables considered for the current investigations are listed in Table 1.

When the number of variables for an experiment is relatively small, the testing can be conducted with all possible combinations to completely understand the combined effect. However, if the number of variables and their variations are high, then it is not feasible to consider all possible combinations. Hence, the combinations are selected that the experimental work can be performed without impeding the achievable understanding. The orthogonal array method (often referred to as Taguchi methods, see e.g. Hedayat *et al*. 1999) is adopted for selecting the most informative combinations. The method can reduce the total cost of experimental works and improve the test efficiency, because the combinations selected reflect the representative coverage

of all possible combinations. The orthogonal array should fulfill two requirements: (1) for each variable and variation the same number of tests is performed; (2) for any two parameters the same number of tests is performed (Ji 2001). These two requirements are called orthogonality which ensures that the distribution of all variables and their variations in tests is uniform.

For an experiment which contains four variables with each variable having three variations, the possible combinations are 81, i.e. 3^4. The orthogonal method recommends then an array of L_9, i.e. a set of nine tests is required. There are 9 rows and 4 columns in the orthogonal array L_9. Each column represents one of the variables, i.e. λ, $N/(f_cA_g)$, ρ_s and ρ_v in Table 2. Each variation will be repeated three times in each column. Each combination, composed of variations in every two columns, appears once. They are (1,1), (1,2), (1,3), (2,1), (2,2), (2,3), (3,1), (3,2), (3,3), where, 1, 2, 3 represent three variations of the variables, respectively. This is because the influence of each variable is unknown before testing is performed. To avoid arranging combinations with extreme variations, it is better to arrange the array at random rather than rank each variation in order of its value (e.g., Hedayat *et al*. 1999). The combinations of design parameters selected from Table 1 are listed in Table 2. Dimensions and reinforcement arrangements of nine specimens are shown in Fig. 2. When arranging the longitudinal reinforcement, the distances should be as uniform as possible. If the number of rebars is too small to have the same distance, the distances are properly adjusted.

Table 1 Parameters of Piers

Variable	Variation		
Height of model pier (H)	1.6	2.0	3.0
Axial load ratio ($N/(f_cA_g)$)* (%)	5	10	15
Longitudinal reinforcement ratio ρ_s (%)	0.15	0.40	0.75
Stirrup-to-concrete volume- ratio ρ_v (%)	0.15	0.30	0.45

*Note: f_c is the axial compressive strength of concrete specimen of 100 × 100 × 300mm; A_g is the concrete gross area, and N is the axial load

Table 2 Combination of variables

Model Number	Height-H (m)	$\lambda=H/T$	$N/(f_cA_g)$ (%)	ρ_s (%)	ρ_v (%)
SOL-1*	1.6	3.6	15	0.75	0.30
SOL-2	1.6	3.6	5	0.15	0.45
SOL-3	1.6	3.6	10	0.40	0.15
SOL-6	2.0	5.3	5	0.75	0.15
SOL-8	2.0	5.3	15	0.40	0.45
SOL-9	2.0	5.3	10	0.15	0.30
SOL-11	3.0	8.0	10	0.75	0.45
SOL-12	3.0	8.0	15	0.15	0.15
SOL-13	3.0	8.0	5	0.40	0.30

*Note: 'SOL' in the model number denotes solid

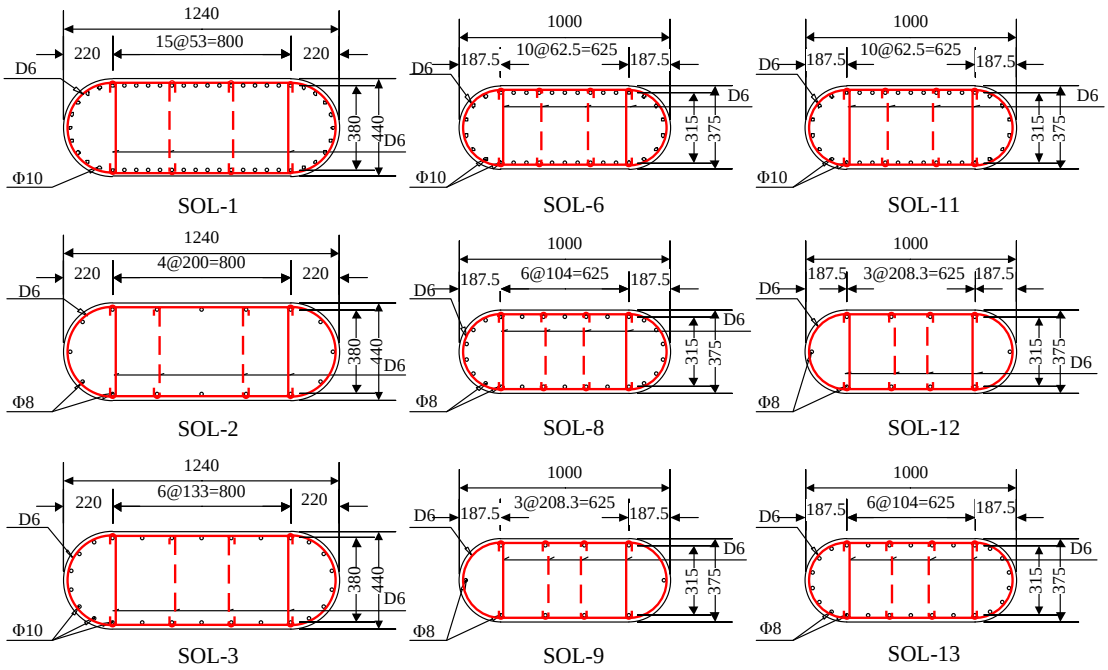

Notes: The unit is mm; D and Φ represent stirrups of HPB 235 plain steel bar and HRB 335 hot rolling ribbed reinforcing bar, respectively

Fig. 2 Dimensions and reinforcement of model piers

2.3 Properties of materials

The design value of compressive strength $f_{cu,k}$, the compressive strength f_{cu} of 150 mm cubic samples, and the axial compressive strength f_c of the samples with the size of 100 mm×100 mm×300 mm are presented in Table 3. An average from samples is taken to obtain a reliable concrete strength. The average compression strength of concrete samples was experimentally determined before performing experiments on each pier.

The longitudinal reinforcement ratio ρ_s of all specimens is between 0.2% and 0.75%. To satisfy the smaller reinforcement ratio and symmetry of specimens, two kinds of rebar with different diameters were adopted. The hot rolling ribbed reinforcing rebars of 8 mm and 10 mm diameter have an average yield strength of 452 MPa and 405 MPa, respectively. The plain steel rebars of 6 mm diameter with an average yield strength of 550 MPa are used as the transverse reinforcement.

2.4 Test setup and loading history

The test setup is shown in Fig. 3. The system includes a 1000 kN horizontal servo actuator to generate the lateral loading with ±300 mm stroke and a 2000 kN manual hydraulic jack to produce the initial constant vertical axial loading. The actuator was attached to the laboratory reaction wall and to a rigid steel cap on top of the specimen. The rate of lateral cyclic loading is 0.005 mm/s with gradually increasing amplitudes shown in Fig. 4. The data acquisition system records

horizontal and vertical displacements, inputs from the strain gauges on stirrups and longitudinal bars, and detects possible translations and rotations at the base. The strain gauges were adhered to the surface of the reinforcement rebars before the specimens were built. The footing size was 2.0 m × 1.5 m × 0.4 m, and was restrained to the strong floor to avoid base displacements and rotations. Before the cyclic loading, each specimen was placed under axial compressive load, about 20% of the lateral load that will initiate crack. The load was applied twice to eliminate the asymmetry of the specimens and to confirm the proper function of the equipment and gauges.

The ultimate displacement is defined as the maximum displacement corresponding to 85% of the maximum strength after reaching the peak value (see also Fig. 7). In Fig. 4, Δ_y is the yield displacement of the longitudinal reinforcement.

Table 3 Compressive strength of concrete (average value)

Model Number	$f_{cu,k}$ (MPa)	f_{cu} (MPa)	f_c (MPa)
SOL-1, SOL-8, SOL-11*	35	43.1	28.8
SOL-2, SOL-6, SOL-13*	35	43.4	26.7
SOL-3, SOL-9, SOL-12*	35	38.6	25.2

*Note: three piers in the same line were casted at the same time and their concrete was same

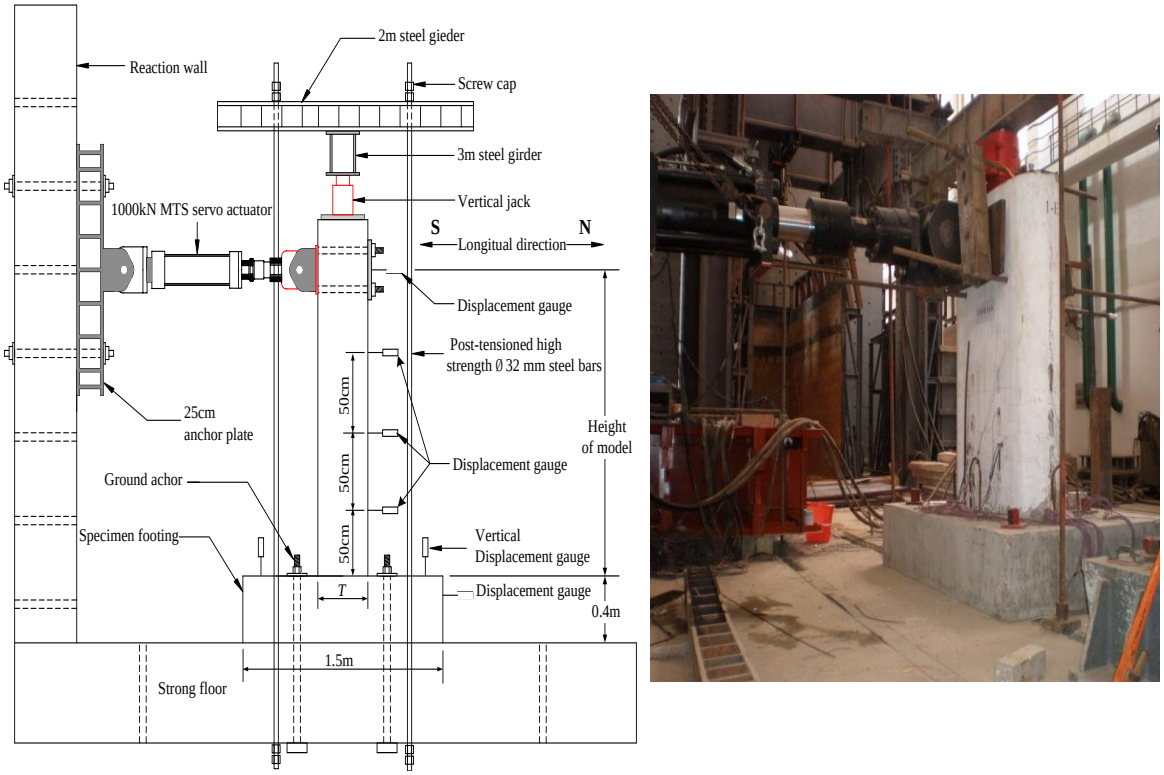

(a) Schematic layout (b) Overview

Fig. 3 Test setup

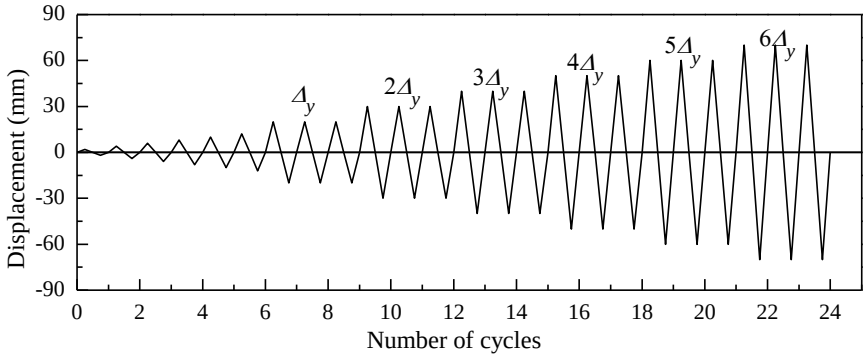

Fig. 4 Displacement loading history

(a) Spalling at the base, SOL-6 pier (b) Crack development, SOL-13 pier

Fig.5 Typical failure of specimens

3. Test results

3.1 Crack and damage behavior

As cracks developed in the specimens, the force-displacement relationship became nonlinear. The first crack was located near the pier support. Cracks propagated from the edge to the middle of the cross-section, and the cracks from both sides finally intersected near the central axis. In the plastic zone, the cracks developed at regular intervals during the entire duration of the cyclic loading, and new cracks developed from the bottom with the same spatial regularity in each subsequent loading cycle. New cracks may not occur in the piers after the stress in the reinforcement reached the yield value. However, existing cracks will likely propagate rapidly. In all cases, the failure mode was bending failure with flexural cracks. When the longitudinal reinforcement ratio of piers is relatively large, the buckling failure of the longitudinal reinforcements was dramatic with concrete crushing and spalling. Stirrups in all specimens did not

yield because of their small strains. The representative failure modes are shown in Fig. 5.

With little reinforcement, the bond slip and the tensile fracture of rebars occurred prior to concrete compressive failure. In addition, the less the longitudinal reinforcement ratio is, the more deeply cracks develop. With the largest longitudinal reinforcement ratio and the smallest stirrup-to-concrete volume- ratio, buckling of rebars and spalling of concrete cover are pronounced in the specimen SOL-6, while other piers have only crack failure. This is because ultimate strain of reinforcement is attained before the spalling of concrete.

3.2 Hysteretic behavior

The hysteretic curves obtained from the low cyclic loading can approximately reflect the seismic performance of specimens. The top horizontal force-displacement curves of the specimens are shown in Fig. 12.

When the specimens were in the elastic range, the deformation almost recovered after unloading, and the area enclosed by the hysteretic loops, which represent energy dissipation, was negligible. When cracks developed, the curve became nonlinear with a declining slope gradient, indicating a stiffness reduction, and the energy dissipation increased gradually. After longitudinal rebars yielded, the horizontal force increased slowly and the stiffness kept degrading. The energy dissipation increased indicating by larger residual displacements after the unloading. During the three-cycle loading with the same displacement (see Fig. 4), the shapes of the hysteretic curves showed only a little change.

The longitudinal reinforcement ratio has a large effect on the shape of the hysteretic curves. The hysteretic loops are wider for the specimens with a larger number of longitudinal reinforcement compared to the other specimens, and ultimately the energy dissipation can be enhanced. For the specimens with a low longitudinal reinforcement ratio, the displacement decreased so dramatically in the early stages of unloading that the stiffness was negligible, i.e. the displacement reduced at a constant force (see e.g. the cases of SOL-2 and SOL-12). However, the unloading stiffness recovered and converged close to the initial stiffness after the displacement dropped. The hysteretic loops of specimens with 0.4% longitudinal reinforcement ratio were narrow compared to the specimens with high longitudinal ratio, and the unloading stiffness was almost constant (see SOL-3 and SOL13).

All specimens failed to demonstrate a good seismic performance because the longitudinal reinforcement ratio was small. The variation in stirrup-to-concrete volume- ratio had only a minor impact on the shape of the hysteretic curves.

3.3 Skeleton curve

The envelope of the force-displacement curve, i.e. the path of the successive peaks by connecting all peak values of the first cycle at each load level, is defined as the skeleton curve (e.g., Sheikh and Khoury 1993). The skeleton curves of the tested specimens with different pier heights are shown in Fig. 6. Skeleton curves initially develop linearly. The initial stiffness of the specimens with larger longitudinal reinforcement ratios is higher compared to that of the other specimens. There is a difference among the peak values of the force, but the shapes of the force-displacement curves are approximately the same.

The skeleton curves of 1.6 m piers differ significantly from each other. The peak force of specimens with a high longitudinal reinforcement ratio ρ_s (SOL-1) is over three times higher than that of the specimens with a low ρ_s (SOL-2). This difference is the combined result of the ratio of axial load to concrete compressive strength $N/(f_c A_g)$ and ρ_s. The bending strength will increase when both variables increase. Both variables in SOL-1 case are three times larger than that of SOL-2 case. Therefore, the peak force of specimen SOL-1 is higher.

For piers of 2 m height, the skeleton curves are less sensitive. The peak forces do not vary much. In the positive direction, the bearing capacities of specimen SOL-6 and specimen SOL-8 are very close, but in the negative direction they are different. A possible cause is that the specimens were not built perfectly symmetrical. The curves in both models decline rapidly after reaching their ultimate limit forces, because the bond slip between concrete and reinforcements reduces the ductility.

Specimen SOL-11, pier of 3 m height, went through a long ascending process from cracking to the peak load and then sudden failure. In contrast, specimen SOL-12 and specimen SOL-13 reached the peak load quickly after the yielding load. After declining slowly, they can experience sudden damage when tensile failure occurs because of less longitudinal reinforcement. The ρ_s of specimen SOL-11 is larger than the two other specimens. Specimen SOL-11 has the larger axial load, and thus the peak load is also higher.

3.4 Displacement ductility

Several definitions of ductility are given in the literature. The displacement ductility adopted is shown in Fig. 7. After determining the skeleton curves and maximum lateral loading F_{max}, the definition of the yield and ultimate displacement is obtained through connecting the origin to the point with the value of 0.75 F_{max} on the skeleton curve and extending the line to intersect the horizontal line indicating the maximum loading. The horizontal coordinate of the intersection point *B* or *D* is the yielding displacement X_y (Priestley and Park 1987). When the loading declines to 0.85 F_{max}, the corresponding displacement is the ultimate displacement X_u. The displacement ductility was defined as μ:

$$\mu = X_u / X_y \tag{1}$$

The displacement ductility is shown in Table 4. The ductility ranges approximately between 3 and 6.

When the variance of the ductility was analyzed for the first time, all variables were considered. Hedayat (1999) recommended that the variable, with the smallest square sum of average deviation among the four considered variables, i.e. with the smallest influence, should be used as an estimate in variance analysis. In the study considered the stirrup-to-concrete volume ratio was the variable with the smallest influence on the displacement ductility. Hence, it is used to evaluate the influence of the other three variables. As shown in Fig. 8, the influence of each variable on the ductility is described after analyzing the variance of the ductility.

The displacement ductility reduces as the ratio of height to thickness and the axial load ratio increase. The stirrup-to-concrete volume ratio has less effect on the ductility. When ρ_s is less than 0.4%, the displacement ductility decreases with an increase of ρ_s. In contrast, the ductility increases slowly when ρ_s is larger than 0.4%.

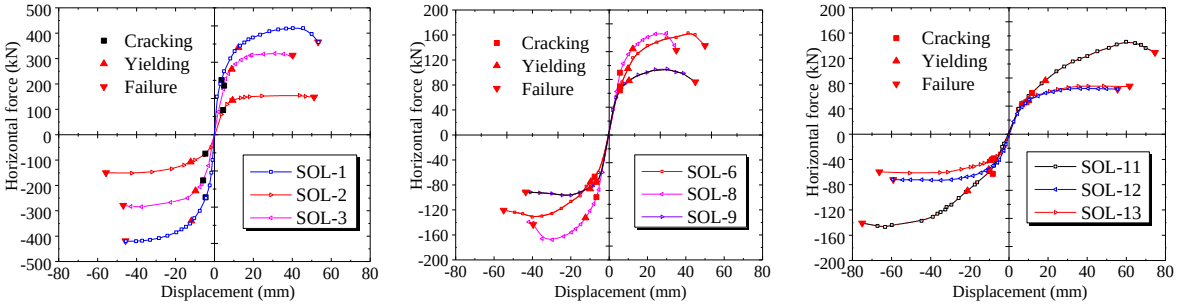

(a) Pier height = 1.6 m (b) Pier height = 2 m (c) Pier height = 3 m

Fig. 6 Effect of pier height and reinforcement ratio on skeleton curves

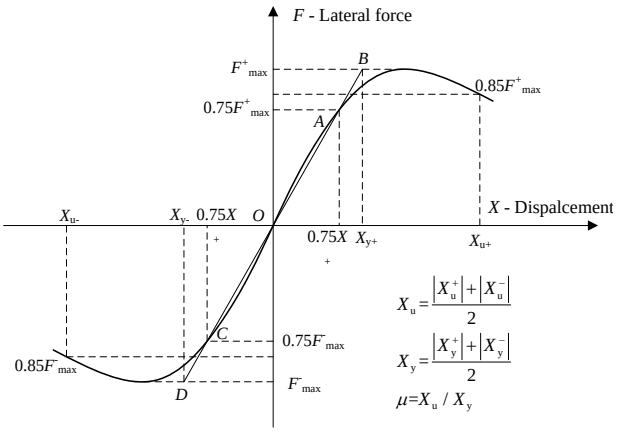

Fig. 7 Definition of the yield and ultimate displacement

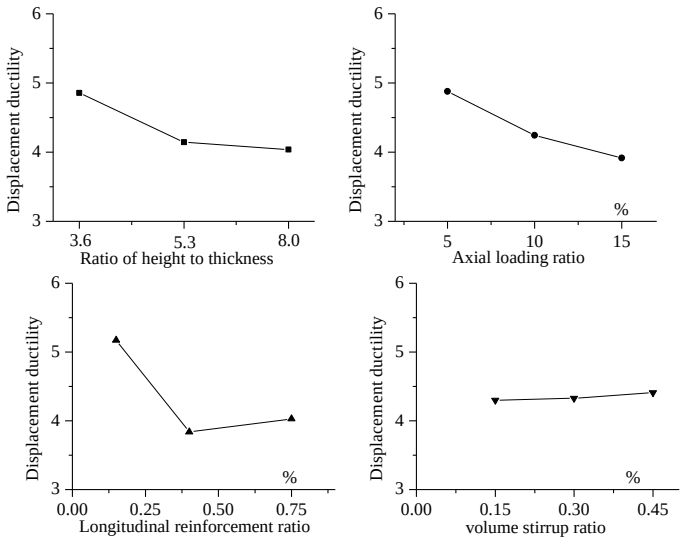

Fig. 8 Influence of considered variables on the displacement ductility μ

Table 4 Displacement ductility of specimens

Number	Direction	Yielding		Failure		Ductility	Average
		Displacement (mm)	Load (kN)	Displacement (mm)	Load (kN)		
SOL-1	+	12.31	343.2	53.27	365.7	4.33	4.09
	-	-11.87	-340.2	-45.69	-418.2	3.85	
SOL-2	+	8.15	130.9	51.19	148.5	6.28	5.53
	-	-11.64	-105.6	-55.68	-149.9	4.78	
SOL-3	+	9.65	265.8	40.22	313.1	4.17	4.20
	-	-11.06	-229.3	-46.81	-278.3	4.23	
SOL-6	+	12.19	117.2	51.20	137.4	4.20	4.31
	-	-12.49	-90.3	-55.22	-110.0	4.42	
SOL-8	+	11.17	132.9	34.77	137.6	3.11	3.27
	-	-11.69	-130.7	-40.13	141.8	3.43	
SOL-9	+	8.73	81.6	43.19	88.9	4.95	4.85
	-	-9.15	-82.1	-43.47	-91.3	4.75	
SOL-11	+	19.50	84.7	74.62	129.3	3.83	3.68
	-	-21.20	-89.7	-75.00	-140.8	3.54	
SOL-12	+	12.87	59.4	55.51	71.2	4.31	4.39
	-	-13.23	-45.8	-59.15	-71.8	4.47	
SOL-13	+	15.73	61.8	61.67	76.2	3.92	4.04
	-	-15.92	-62.9	-66.23	-59.7	4.16	

4. Numerical analysis and discussion

4.1 Constitutive model of materials

The bridge pier of railway for high-speed trains in China has a large cross-section and low longitudinal reinforcement ratio. However, the existing constitutive models of concrete are mainly applicable to piers with a relatively small cross-section and higher longitudinal reinforcement ratios. It is therefore necessary to investigate the suitability of existing concrete constitutive models for bridge piers with large cross-sections and low longitudinal reinforcement ratio. In the following, the existing concrete models are briefly described.

4.1.1 Concrete Model

The accuracy of simulation of pier behavior is strongly determined by the concrete model used, particularly in terms of the unloading and reloading behavior, as well as the residual displacements. The general shape of the concrete stress-strain curve has three parts (Waugh 2009): (1) the initial slope of the curve is the elastic modulus (E_c); (2) the maximum value which shows the peak stress and the corresponding strain (f_c', ε_0, respectively); and (3) post peak behavior. Under the axial load, the concrete section will dilate in the transverse direction due to Poisson's

effect. The dilation will lead to an increase in the strength, strain, and ductility of the concrete section. For unconfined concrete, the curves descend quickly after reaching a peak value. In confined concrete, the rate of the descending branch depends on both the level of the confinement and strength of the concrete.

In this study, the three widely adopted concrete constitutive models, proposed by Kent, Scott and Park, Mander, and Chang and Mander, are used to predict the behavior of concrete columns under low cyclic loading.

Kent-Scott-Park model

In the Kent-Scott-Park model (Scott *et al*. 1982, Mohd Yassin 1994), the monotonic concrete stress-strain relation under the compression loading is described by three regions. Assuming that the compression is positive, the three regions are described as:

$$0 \le \varepsilon_c \le \varepsilon_0, \quad \sigma = Kf_c'\left[2\left(\frac{\varepsilon_c}{\varepsilon_0}\right) - \left(\frac{\varepsilon_c}{\varepsilon_0}\right)^2\right] \tag{2}$$

$$\varepsilon_0 \le \varepsilon_c \le \varepsilon_u, \quad \sigma = Kf_c'[1 - Z(\varepsilon_c - \varepsilon_0)] \tag{3}$$

$$\varepsilon_c > \varepsilon_u, \quad \sigma = 0.2Kf_c' \tag{4}$$

provided: $\varepsilon_0 = 0.002K$, $K = 1 + \rho_{st} f_{yh} / f_c'$, and

$$Z = 0.5 / \left(\frac{3 + 0.29 f_c'}{145 f_c' - 1000} + \frac{3}{4}\rho_{st}\sqrt{\frac{h'}{s_h}} - 0.002K\right)$$

where, ε_0 is the concrete strain at the peak compressive stress f_c'; ε_u is the ultimate strain; f_{yh} is the yield strength of stirrups; ρ_{st} is the ratio of the volume of transverse reinforcement to the volume of concrete core measured at the outside of the stirrups (it is simplified into stirrup-to-concrete volume ratio); h' is the width of concrete core measured at the outside of the stirrups; and s_h is the center to center spacing of the stirrups.

Mander model

Mander *et al*. (1988) have proposed the following stress-strain approach for a confined concrete based on an equation suggested by Popovics (1973):

$$\sigma = f_{cc}' \frac{xr}{r - 1 + x^r} \tag{5}$$

$$\varepsilon_{cc} = \varepsilon_{c0}\left[1 + 5\left(\frac{f_{cc}'}{f_{c0}'} - 1\right)\right] \tag{6}$$

provided: $x = \frac{\varepsilon_c}{\varepsilon_{cc}}$, $r = \frac{E_c}{(E_c - E_{sec})}$, $E_c = 5000\sqrt{f_{c0}'}$, and $E_{sec} = f_{cc}' / \varepsilon_{cc}$

where, f_{cc}' is the peak strength of the confined concrete; f_{c0}' is the peak strength of an unconfined concrete; ε_{cc} and ε_{c0} are the strains at the peak compressive stresses of the confined and unconfined concrete, respectively; and r is a parameter controlling the shape of the curve. E_c is the initial slope of curve.

Chang-Mander model

Chang and Mander (1994) extended the Mander model and investigated a number of curves for describing the envelope response. Waugh (2009) has later improved the model. The modified model, called the Chang-Mander model, is described in the following for an unconfined concrete.

$$x = \varepsilon_c / \varepsilon_{c0} \tag{7}$$

$$y = \sigma_c / f_c' \tag{8}$$

$$\text{or } y = \frac{nx}{1+(n-\frac{r}{r-1})x+\frac{x^r}{r-1}} \tag{9}$$

with $r = f_c'/5.2-1.9$, $n = E_c\varepsilon_{c0} / f_c'$, $E_c = 8200(f_c')^{3/8}$ and $\varepsilon_{c0} = (f_c')^{1/4}/1153$

where, r and n are the parameters to control the shape of the curve.

Chang and Mander (1994) also proposed the following equations to calculate the increase in the peak strength of confined concrete:

$$f_{cc}' = f_{c0}'(1+k_1\, x') \tag{10}$$

$$\varepsilon_{cc}' = \varepsilon_{c0}'(1+k_2\, x') \tag{11}$$

Waugh (2009) provided the following

$k_1 = A\left(0.1+\frac{0.9}{1+Bx'}\right)$, $x' = \frac{f_{l1}+f_{l2}}{2f_{c0}}$,

$A = 6.886-(0.6069+17.275r)e^{-4.989\gamma}$, $B = \frac{4.5}{\frac{5}{A}(0.9849-0.6306e^{-3.8939\gamma}-0.01}$

$\gamma = f_{l1}/f_{l2}$, $k_2 = 5k_1$, $f_{lx} = \rho_x f_{yh}$, $f_{ly} = \rho_y f_{yh}$, $n = \frac{E_c\varepsilon_{cc}}{f_{cc}'}$, and $r = \frac{n}{n-1}$

where, f_{l1} and f_{l2} are respectively the transverse confining stress in two directions.

4.1.2 Comparison of the three models

The three models, proposed by Kent, Scott and Park, Mander, and Chang and Mander, are compared in Fig. 9. When the concrete is subjected to a compression loading, the shapes of the curves, obtained from the three models, are basically the same between the origin and the peak stress. After reaching the peak stress, the curves vary considerably, with the Mander model predicting higher stress and the Chang- Mander model predicting lower stress.

The typical hysteretic behavior under compressive stress is characterized by the secant modulus $E_{sec} = f_c'/\varepsilon_c'$, and the initial modulus E_{new} under the reloading. The cycle of unloading and reloading behavior in Kent-Park model and Mander model is represented by a set of straight lines. In contrast, the behavior of the Chang-Mander model is a set of curves, which is more complicated.

4.1.3 Steel model

Giuffré-Menegotto-Pinto model, presented by Filippou *et al*. (1983) and Faria *et al*. (2004), describes the hysteretic behavior of reinforcing bars, as shown in Fig. 10. The model includes (1) the Bauschinger's effect activated under a cyclic loading and (2) the axial behavior of each rebar.

The constitutive model is adopted here with reference to the notation of Fig. 10, and defining E_s and E_{sh} as the elastic and the hardening modulus of steel, respectively. The following equation describes the stress-strain relationship (Faria *et al*. 2004)

$$\frac{\sigma-\sigma_r}{\sigma_I-\sigma_r}=\left(\frac{E_{sh}}{E_s}+\frac{1-E_{sh}/E_s}{[1+\varepsilon^{*R}]^{R^{-1}}}\right)\varepsilon^{*} \tag{12}$$

$$R=R_0-\frac{a_1+\xi}{a_2+\xi},\quad \xi=\frac{\varepsilon_{r\max}-\varepsilon_I}{\varepsilon_I-\varepsilon_r}\ \text{and}\ \varepsilon^{*}=\frac{\varepsilon-\varepsilon_r}{\varepsilon_I-\varepsilon_r}$$

where, $\varepsilon_{r\max}$ represents the maximum reversal strain that ε_r reached; the model parameters R_o, a_1, and a_2 are defined according to the stress-strain curves obtained in the experimental characterization tests.

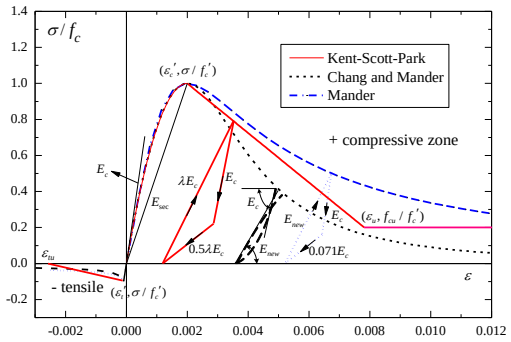

Fig.9 Comparison of the three models

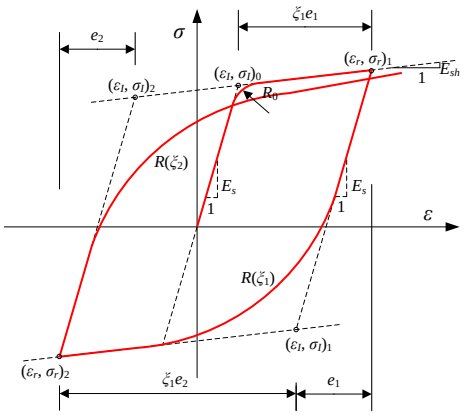

Fig. 10 Giuffré-Menegotto-Pinto steel model

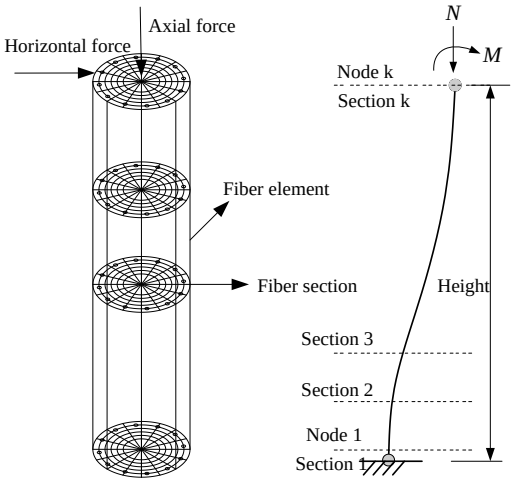

Fig.11 Analysis model at the fiber section level

4.2 Analysis method

The piers can be numerically simulated at three levels - the section level, the three-dimensional element level, and the fiber section level (see e.g. Taucer *et al*. 1991). At the section level, the moment curvature relationship of the section is required. The approach is simple. However, it provides only a rough estimate. With a three-dimensional element, a large number of finite elements are required and all parameters in the constitutive model need to be determined. This will require more computational memory and time, and the analysis may not converge. Not only does the fiber section method take less time to analyze, it is also convenient to establish a numerical model.

The fiber section approach will be applied in this study. Since two different materials are involved in each pier, the section should be discretized as accurate as possible. A patch fiber is used to represent concrete fibers, while individual fibers simulate the steel reinforcements. Subsequently, the corresponding uniaxial stress-stain relationships are provided. The nodes of the individual fiber sections associated with both materials are linked rigidly, and thus possible bond-slip is ignored for simplicity. The analytical model is shown in Fig. 11, and assumes that the strains in fiber section are based on Euler–Bernoulli assumptions, i.e., plane sections remain plane. The software OpenSees developed at the University of California at Berkeley was used to analyze the force-displacement of the specimens using the detailed material parameters. OpenSees has a section aggregator which can overlap shear and normal stresses, but there is no interaction between responses in different degrees-of-freedom directions.

4.3 Comparison between numerical and experimental results

The hysteretic curves of specimens analyzed with the three models, i.e. Kent-Scott-Park, Mander, and Chang-Mander models, were compared with the experimental results in Fig. 12. The skeleton curves of the force-displacement relationship were also evaluated. The experimental results are indicated by a solid line, while the numerical values are displayed by a dashed line.

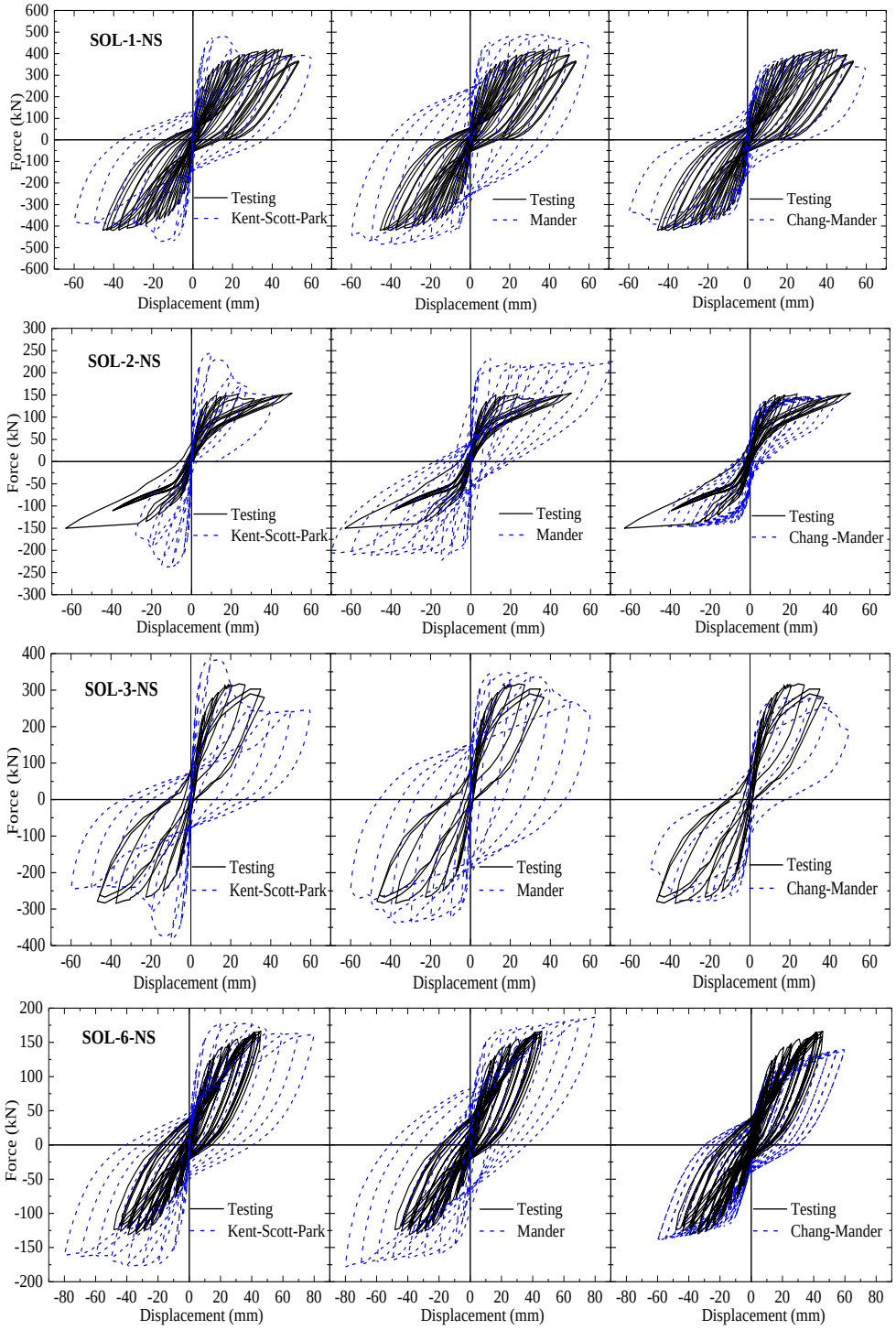

Fig. 12 continued

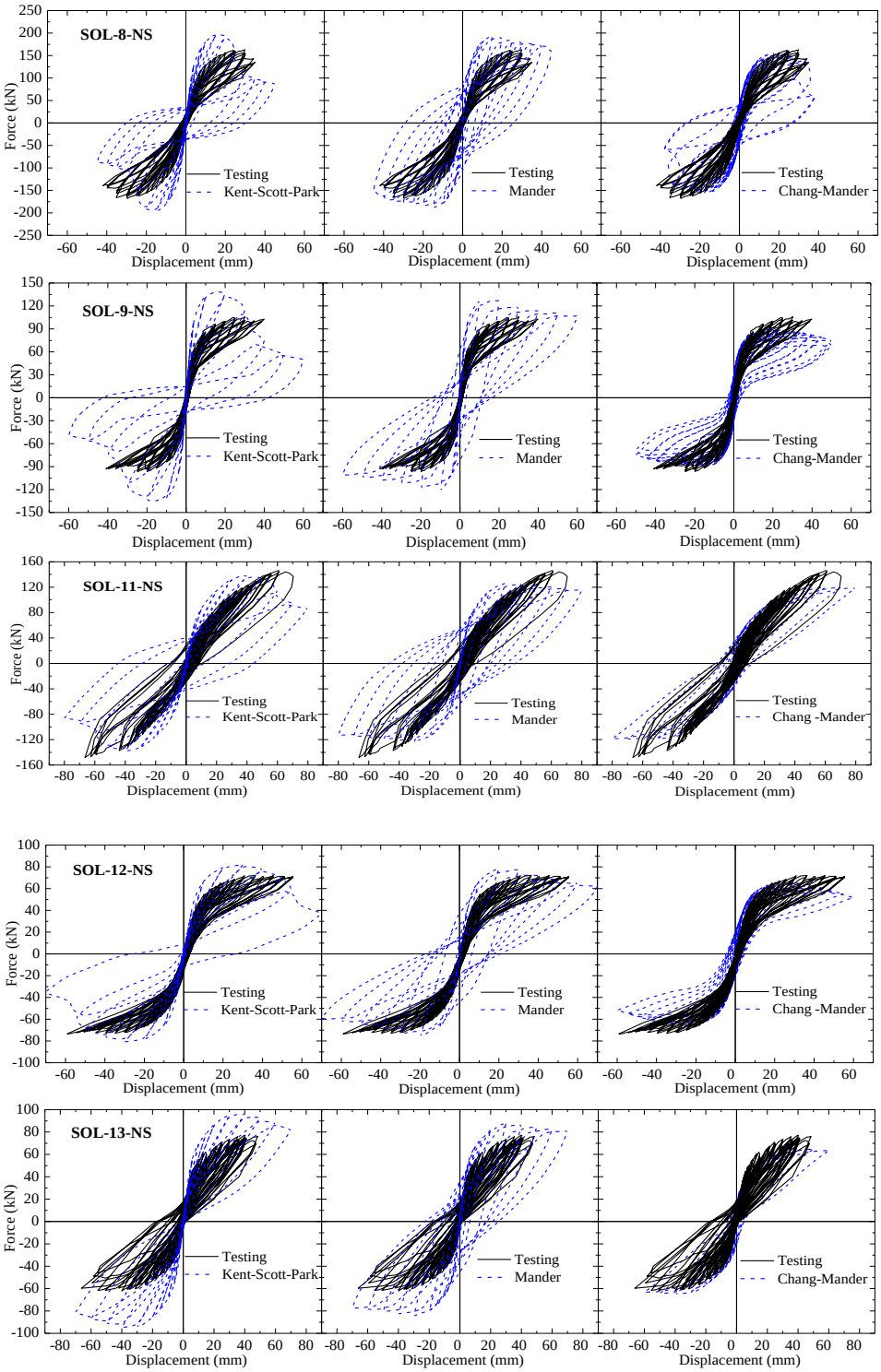

Fig. 12 Consequence of selected concrete model for the predicted force-displacement curves

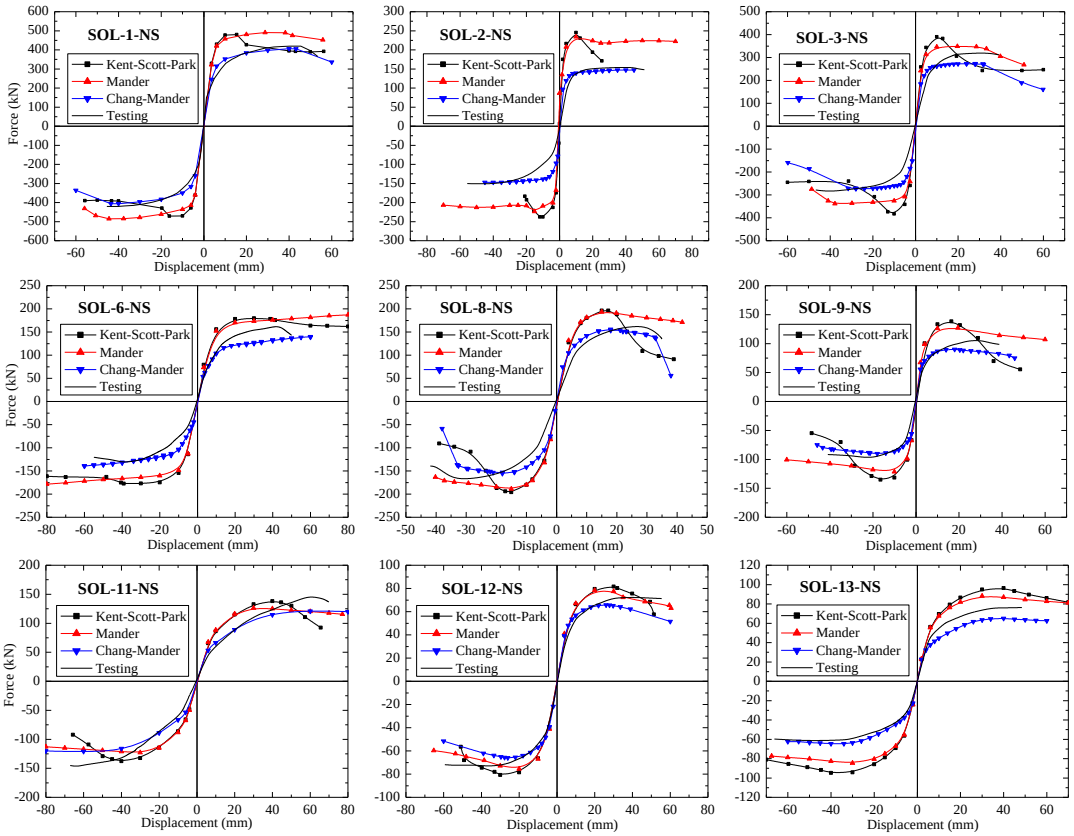

Fig. 13 Influence of the concrete model used on the force-displacement relations

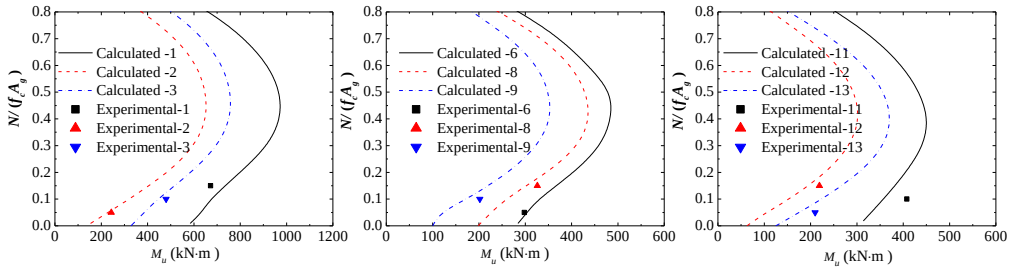

(a) Pier height = 1.6 m (b) Pier height = 2.0 m (c) Pier height = 3.0 m

Fig. 14 Simultaneous effect of aspect, axial load and reinforcement ratios on N-M relationship

In most cases, the skeleton curves obtained using the Chang-Mander model match the experimental results well. However, the curves of the other two models (the Kent-Park model and Mander model) are significantly different from the experimental results, particularly regarding the peak force and the later degradation of the curves.

The Chang-Mander model takes into account more influence factors and energy-dissipation quantities so that its result was more appropriate. It is worthwhile mentioning that the area enclosed by an analyzed single cycle is larger than that obtained from experiments, although their

shapes are similar. This is because the bond slip between the concrete and the reinforcement may occur. Hence, some energy dissipation may take place. However, Chang-Mander model does not consider the bond-slip effect. For specimens with lower reinforcement ratio, the Kent-Scott-Park model and Mander model are unable to predict the experimental results, especially the unloading path. From the description of the two concrete models, their unloading curves keep a straight line all the time and fail to reflect a change in stiffness.

The comparison shows that the cyclic behavior of the pier is significantly influenced by the longitudinal reinforcement ratio. Specimens SOL-1, SOL-6 and SOL-11 with 0.75% longitudinal reinforcement ratio show a fuller hysteretic loop than that of other specimens. Among the three concrete models, the Mander model has the largest residual displacements and dissipates more energy due to the higher unloading stiffness. In most of the cases, the residual displacements using the Kent-Scott-Park model were smaller than the Mander model, and the strength of Kent-Scott-Park model decreases quickly. As a result, the ductility with the Kent-Scott-Park model is the smallest.

The hysteretic curves of specimens with 0.4% longitudinal reinforcement ratio become narrow. All concrete models predict a pinching phenomenon correctly while analyzing specimen SOL-3, SOL-8 and SOL-13.

The analytical hysteretic curves of specimens with 0.15% longitudinal reinforcement ratio are the narrowest (see the cases SOL-2, SOL-9 and SOL-12). The straight unloading curves of the Kent-Scott-Park model and Mander model have never been able to match the experimental results. However, the Chang-Mander model agrees with the experimental results well.

The relationship between lateral force and lateral displacement analyzed using the three models are presented in Fig.13. The Chang-Mander model are close to the test results, but the Kent-Scott-Park model and the Mander model predicted larger forces than those from experiments. The initial slopes of the three models are basically the same. Because the confined concrete in the Mander model maintains strength for a longer period, the analytical displacement ductility is largest among the three models. In contrast, the Kent-Scott-Park model has the smallest ductility.

4.4 Axial load and Moment interaction

The interaction between axial load and moment (*N-M*) is shown in Fig. 14. $N/(f_cA_g)$ represents the axial load ratio, and M_u is the maximum moment at the footing. All of the calculated *N-M* curves were analyzed using the Chang-Mander model. Each specimen has different design parameters including the height to thickness ratio (*H*/*T*), and the longitudinal and transverse reinforcement ratio. Thus, to have the total curve, every case requires a number of calculations. It is shown that most of the calculated analyses matched the experimental results well.

The peak moments at the footings are significantly affected and increase with increasing longitudinal reinforcement ratio. In the 1.6 m specimens, the numerical moments of specimens SOL-2, SOL-3 are a little higher than the tested results, but for the numerical moments of specimen SOL-1, the opposite is the case. In the 2.0 m specimens, specimens SOL-8, SOL-9 are a little lower than the tested results. In the 3.0 m specimens, the analytical moments of specimens SOL-12, SOL-13 are similar to the experimental results. However, the moment of specimen SOL-11 from experiments is larger than the numerical result. This is possibly because SOL-11 has more reinforcement which makes the confined concrete stronger than the calculated one.

The values obtained from the experiments are lower since the variation of axial forces in all considered specimens is very low. The analyses show that the bending moment will have the largest value when the axial load ratio is in the range between 0.4 and 0.5. In all other axial load ratios, the bending moment will have a smaller value.

5. Conclusions

Cyclic tests on nine model piers were carried out and failure characteristics, hysteresis curves, and skeleton curves were obtained. Three concrete models and a steel model were applied to analyze the hysteretic response of these specimens. To identify the most suitable material model, the numerical results were compared with the experimental results.

The experimental results show that:

When the ratio of longitudinal reinforcement is high, the cracks spread out more intensively. In contrast, with less reinforcement, the bond slip between reinforcement and concrete takes place, and the tensile fracture of reinforcement occurs prior to the concrete spalling because of crushing in the compression zone.

For piers of the same height and cross-section, the bearing capacities will improve with increasing longitudinal reinforcement ratio and axial load ratio. Alterations of stirrup-to-concrete volume ratio have less effect on the hysteretic curves. Specimens display poor displacement ductility.

Models with less than 0.4% of longitudinal reinforcement ratio pinch severely near the origin of the hysteretic curves. Although the displacement level increases, the energy dissipation increases slowly and the stiffness of the curves changes sharply during the unloading phase.

The comparison between numerical and experimental results reveal:

Chang-Mander model predicted the experimental data most accurately. The results obtained using the Kent-Scott-Park model and Mander model were higher than the tested values. Furthermore, Chang-Mander model could also predict the various stiffness values during the unloading phase.

Acknowledgements

This research was supported by the Railways Ministry of China (under contract number 2009G-024) and the National Engineering Laboratory for Construction Technology of High Speed Rail in China, and this is gratefully acknowledged. The authors are also very grateful to the China Scholarship Council for their support of the first author's PhD research and research at the University of Auckland, New Zealand.

References

Belarbi, A., Prakash, S. and You, Y.M. (2009), "Effect of spiral reinforcement on flexural-shear-torsional seismic behavior of reinforced concrete circular bridge columns", *Struct. Eng. Mech.*, **33**(2), 137-158.

Berry, M., Parrish, M. and Eberhard, M. (2004), *PEER Structural Performance Database User's Manual*, Pacific Earthquake Engineering Research Center, Berkeley, California, USA.

Braga, F., Gigliotti, R. and Laterza, M. (2006). "Analytical stress–strain relationship for concrete confined by steel stirrups and/or FRP jackets", *ASCE J. Struct. Eng.*, **132**(9), 1402-1416.

Chang, G.A. and Mander, J.B. (1994), *Seismic Energy Based Fatigue Damage Analysis of Bridge Columns: Part 1-Evaluation of Seismic Capacity*, Report No. NCEER-94-0006, State University of New York, Buffalo, New York, USA.

Chen, W.F. and Duan, L. (2003), *Bridge Engineering: Seismic Design*, CRC Press, Boca Raton, Florida, USA.

D'Amato, M., Braga, F., Gigliotti, R., Kunnath, S. and Laterza, M. (2012), "A numerical general-purpose

confinement model for non-linear analysis of R/C members", *Comput. Struct.*, **102-103**(7), 64-75.
Faria, R., Pouca, N.V. and Delgado, R. (2004), "Simulation of the cyclic behavior of R/C rectangular hollow section bridge piers via a detailed numerical model", *J. Earthq. Eng.*, **8**(5), 725-748.
Filippou, F.C., Popov, E.P. and Bertero, V.V. (1983), *Effects of Bond Deterioration on Hysteretic Behavior of Reinforced Concrete Joints*, Report No. EERC 83-19, Earthquake Engineering Research Center, University of California at Berkeley, Berkeley,CA.
Fujikura, S., Kawashima, K., Shoji, G., Zhang, J. and Takemura, H. (2000), "Effect of the interlocking ties and cross ties on the dynamic strength and ductility of rectangular reinforced concrete bridge columns", *J. Struct. Mech. Earthq. Eng.*, **640**(I-50), 71-88.
Hedayat, A.S., Sloane, N.A.J. and Stufken, J. (1999), *Orthogonal Arrays: Theory and Applications*, Springer, New York, USA.
Ji, Z.Y. (2001), *The Method and Theory of Orthogonal Design*, Science and Technology across the World Press, HongKong, China.
Jia, H. and Dai, H. (2012), "Numeric analysis on seismic performance of RC round-ended piers with HRBF500 steel bars", *Appl. Mech. Mater.*, **226-228**, 1577-1580.
Jia, H.M. (2008), "Seismic performance of round end pier in passenger railway", Ph.D. Dissertation, Beijing Jiaotong University, Beijing. (in Chinese).
Ju, Y.Z. (2004), "Study on seismic performance of round-ended railway bridge piers with low longitudinal steel ratio", Ph. D. Dissertation, Beijing Jiaotong University, Beijing. (in Chinese)
Kent, D.C. and Park, R. (1971), "Flexural members with confined concrete", *ASCE J. Struct. Div.*, **97**(7), 1969-1990.
Mander, J.B, Priestley, M.J.N and Park, R. (1983), "Behaviour of ductile hollow reinforced concrete columns", *Bull. NZSEE*, **16**(4), 273-290.
Mander, J.B., Priestley, M.J.N. and Park, R. (1988), "Theoretical stress-strain model for confined concrete", *ASCE J. Struct. Eng.*, **114**(8), 1804-1825.
Mohd Yassin, M.H. (1994), "Nonlinear analysis of prestressed concrete structures under monotonic and cycling loads", Ph.D. Dissertation, University of California, Berkeley, Berkeley.
OpenSees (Open system for earthquake engineering simulation), http://opensees.berkeley.edu/.
Osorio, E., Bairan, J.M. Baira´n, J.M. and Mari´, A.R. (2013), "Lateral behavior of concrete under uniaxial compressive cyclic loading", *Mater. Struct.*, **46**(5), 709-724.
PEER Structural Performance Database, http://nisee.berkeley.edu/spd/.
Popovics, S. (1973), "Numerical approach to the complete stress-strain curve of concrete", *Cement Concr. Res.*, **3**(5), 583-599.
Priestley, M.J.N. and Park, R. (1987), "Strength of ductility of concrete bridge columns under seismic loading", *ACI Struc. J.*, **84**(S8), 61-76.
Scott, B.D., Park, R. and Priestley, M.J.N. (1982), "Stress-strain behavior of concrete confined by overlapping hoops at low and high strain rates", *J. ACI*, **79**(2), 13-27.
Sheikh, S.A. and Khoury, S.S. (1993), "Confined concrete columns with stubs", *ACI Struct. J.*, **90**(4), 414-431.
Sigmund, V. and Penava, D. (2014), "Influence of openings, with and without confinement, on cyclic response of infilled R-C frames - an experimental study", *J. Earthq. Eng.*, **18**(1), 113-146.
Taucer, F.F., Spacone, E. and Filippou, F.C. (1991), *A Fiber Beam-Column Element for Seismic Response Analysis of Reinforced Concrete Structures*, Report No. EERC 91/17, University of California at Berkeley, Berkeley, CA.
Waugh, J. (2009), "Nonlinear analysis of T-shaped concrete walls subjected to multi-directional displacements", Ph.D. Dissertation, Iowa State University, Ames, IA.
Zheng, J. (2008), *Railway Bridge for High Speed Trains in China*, China Higher Education Press, Beijing, China. (in Chinese)